Comprehensive study of the low-temperature transport properties of polycrystalline Sn1+xTe (x = 0 and 0.03)

Dorra Ibrahim, Christophe Candolfi, Sylvie Migot, Jaafar Ghanbaja, Anne Dauscher, Gérard Le Caër, Bernard Malaman, Christopher Semprimoschnig, Bertrand Lenoir

▶ **To cite this version:**

Dorra Ibrahim, Christophe Candolfi, Sylvie Migot, Jaafar Ghanbaja, Anne Dauscher, et al.. Comprehensive study of the low-temperature transport properties of polycrystalline Sn1+xTe (x = 0 and 0.03). Physical Review Materials, 2019, 3 (8), 10.1103/PhysRevMaterials.3.085404 . hal-02303233

HAL Id: hal-02303233

https://univ-rennes.hal.science/hal-02303233

Submitted on 24 Mar 2020

HAL is a multi-disciplinary open access archive for the deposit and dissemination of scientific research documents, whether they are published or not. The documents may come from teaching and research institutions in France or abroad, or from public or private research centers.

L'archive ouverte pluridisciplinaire **HAL**, est destinée au dépôt et à la diffusion de documents scientifiques de niveau recherche, publiés ou non, émanant des établissements d'enseignement et de recherche français ou étrangers, des laboratoires publics ou privés.

Comprehensive study of the low-temperature transport properties of polycrystalline $Sn_{1+x}Te$ (x = 0 and 0.03)

Dorra Ibrahim[1], Christophe Candolfi[1,*], Sylvie Migot[1], Jaafar Ghanbaja[1], Anne Dauscher[1], Gérard Le Caër[2], Bernard Malaman[1], Christopher Semprimoschnig[3], Bertrand Lenoir[1,*]

[1] *Institut Jean Lamour, UMR 7198 CNRS – Université de Lorraine, 2 allée André Guinier-Campus ARTEM, BP 50840, 54011 Nancy Cedex, France*

[2] *Institut de Physique de Rennes, UMR UR1-CNRS 6251, Université de Rennes I, Campus de Beaulieu, 35042 Rennes Cedex, France*

[3] *European Space Agency, ESTEC, P.O. Box 299, Keperlaan 1, 2200 AG Noordwijk, The Netherlands*

[*]Contact authors: christophe.candolfi@univ-lorraine.fr; bertrand.lenoir@univ-lorraine.fr

Abstract

We report on a detailed investigation of the low-temperature transport properties (5 – 300 K) on polycrystalline samples of $Sn_{1+x}Te$ (x = 0 and 0.03) prepared by melt-quenching in water and slow cooling. These two different synthetic routes results in variations in the hole concentration over more than one order of magnitude, allowing for a systematic investigation of the influence of Sn vacancies on the transport properties. The results evidence a strong correlation between the details of the synthetic process and the concentration of Sn vacancies. Transmission electron microscopy and Mössbauer spectroscopy shows that the excess Sn, which helps to lower the hole concentration, segregates at grain boundaries. Interestingly, Hall

effect measurements reveal that charge transport is dominated near 300 K by alloy scattering regardless of the hole concentration. In addition to dictating the electronic properties, the concentration of Sn vacancies has also a significant impact on the thermal transport, with the magnitude of the low-temperature Umklapp peak observed in the lattice thermal conductivity near 30 K scaling with the concentration of Sn vacancies that act as efficient point-defect scatterers.

Introduction

The possibility of converting a thermal gradient into useful electrical power and vice versa makes thermoelectric modules an attractive solid-state technology for waste-heat recovery and coolers.[1,2] This technology requires thermoelectric materials with high efficiency which is determined by the dimensionless thermoelectric figure of merit $ZT = \alpha^2 T/\rho\kappa$ where α is the thermopower or Seebeck coefficient, ρ is the electrical resistivity, κ is the total thermal conductivity and T is the absolute temperature.[1,2] Among the families of thermoelectric materials, PbTe-based compounds, which crystallize in a simple face-centered cubic rocksalt structure, have for long been the materials of choice for powering deep-space probes and rovers.[2] Over the last decade, these materials have attracted further attention with the aim at further enhancing their thermoelectric performances through band-structure engineering or nanostructuring.[3-6]

Compared to PbTe, the isostructural analogue SnTe has received much less attention, largely due to its inherent Sn vacancies that act as double electron acceptor and make it naturally heavily hole doped.[7-28] Early studies on the Sn-Te phase diagram have reported that the Te concentration can vary appreciably between 50.1 and 51.1 at% resulting in significantly inferior thermoelectric performances than those achieved in PbTe.[29-32] Recently, this binary

chalcogenide has reemerged as an interesting Pb-free alternative to PbTe. The electronic band structure of both compounds features strong similarities with the notable presence of two, non-degenerate valence bands that contribute to transport at high temperatures.[33-35] The above-mentioned Sn vacancies and the larger energy offset between these two valence bands in SnTe compared to PbTe are the two main characteristics that distinguish both compounds.[29-35] A large body of studies have shown that SnTe exhibits a rich chemistry with many elements substituting for either Sn or Te.[7-28] These elements can help to compensate holes provided by the Sn vacancies and, meanwhile, to enhance the convergence of the two valence bands, beneficial for achieving high thermoelectric performances at high temperatures. Another widely-used strategy to lower the vacancy concentration is to intentionally introduce excess Sn in the nominal composition, that is, starting from $Sn_{1+x}Te$ compositions with $x \leq 0.03$.[7-28]

Unlike PbTe for which the transport properties have been thoroughly studied down to liquid helium temperatures, little is known on the low-temperature transport properties of $Sn_{1+x}Te$. Herein, we explore in detail the low-temperature transport properties of the binary $Sn_{1+x}Te$ for x = 0 and 0.03 prepared by direct quenching of the melt and slow cooling. For comparison purposes, data collected on a sample prepared by melt-spinning have been added.[36] These three distinct synthetic routes enable tuning the hole concentration over more than one order of magnitude in agreement with pioneering studies on SnTe.[29-33] Surprisingly, the Hall mobility μ_H does not follow the T^{-1} dependence characteristic of acoustic phonon scattering in degenerate systems and usually assumed to prevail in SnTe. Our results evidence that μ_H shows a $T^{-1/2}$ law that persists across the entire concentration range indicating that the electronic transport is dominated by alloy scattering attributed to the atomic disorder caused by the Sn vacancies.

Experimental Section

Synthesis

Polycrystalline samples of $Sn_{1+x}Te$ (x = 0.0 and 0.03) were synthesized by powder metallurgy using stoichiometric quantities of pure Sn (99.999%) and Te shots (99.999%). Prior to use, both elements were purified in order to eliminate possible traces of oxygen. Sn was washed in successive baths of hydrochloric acid diluted in water and a mixture of ethanol and distilled water. Te was purified at 500°C in a silica tube sealed under inert atmosphere (He/H_2). For all samples, stoichiometric weights of purified Sn and Te were loaded into silica tubes sealed under secondary vacuum. The sealed tubes were heated in a rocking furnace to 860°C in 10h. After 5h at 860°C, the tubes were either quenched in room-temperature water or allowed to slowly cool down by switching off the furnace. Details about the melt-spinning process can be found in Ref. 36. Unless otherwise specified, the notation $Sn_{1+x}Te$ with the nominal x values will be used hereafter to label the samples.

The obtained ingots were ground into fine powders which were densified by spark plasma sintering in graphite dies at 500°C for 5 minutes under a pressure of 65 MPa. For all samples, the experimental density of the consolidated ingots, determined by weight and geometrical dimensions, were above 95% of the theoretical density from X-ray diffraction data.

Structural and chemical characterizations

Powder X-ray diffraction (PXRD) was performed on powders both prior and after SPS at 300 K using a Bruker D8 Advance diffractometer ($CuK\alpha_1$ radiation) in reflection mode. Rietveld refinements were performed using the Fullprof software.[37] The spatial distribution of

the elements and the possible presence of secondary phases were assessed by scanning electron microscopy (SEM) coupled with energy dispersive spectroscopy (EDS). Transmission electron microscopy (TEM) was performed on the quenched sample $Sn_{1.03}Te$ in order to determine the localization of the excess Sn. Thin slices were prepared from the consolidated samples by the dual focused ion beam (FIB) – scanning electron microscope system using the in situ lift-out technique. Scanning TEM (STEM) in high-angle annular dark-field (HAADF) mode, annular bright-field (ABF) and high-resolution TEM (HRTEM) were carried out using a JEOL ARM 200F – cold FEG TEM/STEM microscope which operates at 200 keV. The microscope is equipped with a spherical aberration probe (Cs) and image correctors.

^{119}Sn Mössbauer spectra were measured at 300 and 4.2 K, in order to exalt the response of possible Sn^0-containing phase, in transmission geometry with a spectrometer operating in the constant-acceleration mode. A $Ba^{119m}SnO_3$ source (strength of ~10 mCi) operating at 300 K was utilized. ^{119}Sn isomer shifts (IS) are given with respect to $BaSnO_3$ at 300 K and quadrupole splittings are denoted as QS. A mass of 12 mg of powdered samples was used on a surface of 1.75 cm^2. Mössbauer spectra were fitted with a least-squares method assuming Lorentzian peaks. Further details about the analysis of the Mössbauer data can be found in the Supplemental Material.

Transport properties measurements

For transport property measurements, samples were cut from the consolidated ingots with a diamond-wire saw. At low temperatures (5 – 300 K), the electrical resistivity, thermopower and thermal conductivity were measured simultaneously using the thermal transport option (TTO) of a physical property measurement system (PPMS, Quantum Design). Good thermal

and electrical contacts were realized by attaching four copper bars onto a bar-shaped sample (~ 1.5×1.5×8 mm^3) using a small amount of silver epoxy.

Hall effect measurements were performed on bar-shaped samples with a five-probe configuration between 5 and 300 K under magnetic fields $\mu_0 H$ ranging between –1 and +1T using the ac transport option of the PPMS. Ohmic contacts were achieved by brazing copper wires onto the sample with a low-melting-point braze. The Hall resistivity ρ_H was determined from measurements of the transverse resistivity ρ_{xy} under magnetic field reversal following the formula $\rho_H = \left[\rho_{xy}(+\mu_0 H) - \rho_{xy}(-\mu_0 H)\right]/2$. The Hall coefficient R_H was derived from the slope of the $\rho_H(\mu_0 H)$ data assuming a Hall factor r_H equal to unity ($p_H = r_H/R_H e$ where p_H is the Hall hole concentration and e is the elementary charge). In the field and temperature ranges covered here, no deviations of the $\rho_H(\mu_0 H)$ data from linearity was observed.

Results

Phase purity and localization of excess Sn in $Sn_{1+x}Te$

Regardless of the synthetic conditions used, all the samples crystallize in the rocksalt cubic crystal structure of SnTe. The lattice parameters, inferred from Rietveld refinements against the PXRD patterns, are consistent with those determined in prior studies (Table 1).[7-36] In particular, the unit cell parameter *a* tends to increase with increasing the Sn excess, which suggests a decrease in the vacancy concentration. For samples with the highest Sn excess (x = 0.03), additional reflections corresponding to elemental Sn are visible. These reflections disappear after the SPS treatment but without leading to a change in the lattice parameter within experimental uncertainty, indicating that no additional Sn has been inserted into the unit cell.

Given that stoichiometric SnTe is not thermodynamically stable according to the Sn –

Te phase diagram,[38-41] all the samples synthesized should possess elemental Sn in their microstructure. While the very small amount of excess Sn makes these areas invisible in SEM experiments, our TEM investigations clearly evidence that elemental Sn is located at the grain boundaries in samples prepared by melt-quenching (Figure 1a; Ref. 42). These results show that similar Sn-rich areas are also likely present in the other SnTe samples, the amount of which depends on the Sn excess introduced in the nominal composition. The diffraction patterns taken at different zones indicate the absence of short-range vacancy ordering and are thus consistent with a random distribution of Sn vacancies within the SnTe matrix. These conclusions are further corroborated by the ^{119}Sn Mössbauer spectrum recorded at 4.2 K (Figure 1b, left panel), which is in agreement with prior Mössbauer studies performed on this compound.[43-45] A slight asymmetry on the left of the main peak is due to the presence of a small amount of elemental Sn^0. The presence of the characteristic doublet of Sn^0 can be better appreciated on the sharpened spectrum shown in the right panel of Figure 1b (see Ref. 42 for additional details about this procedure). These results demonstrate that elemental Sn is present in the melt-quenched $Sn_{1.03}Te$ sample in addition to a minute amount of SnO_2.

Low-temperature transport properties of $Sn_{1+x}Te$

The temperature dependences of the electrical resistivity of the two series are shown in Figures 2a and 2b. As expected from the heavily-doped nature of these materials, all the samples are metallic with a negligible influence of the synthesis process on the low-temperature behavior. At 300 K, the ρ values are correlated to the Sn concentration and increase from 1.2 to 1.5 μΩ.m upon introducing Sn excess (x = 0.03) for both series. The small hump visible near 100 K coincides with the ferroelectric transition which is accompanied by a cubic-to-rhombohedral distortion of the lattice.[46-48] The fact that this transition is not visible in all

samples is in agreement with prior studies showing that this transition is strongly sensitive to the hole concentration.[46,49]

This trend is confirmed by the temperature dependence of the apparent hole concentration p_H (Figures 3a and 3b). p_H is very sensitive to the synthetic route with a difference of more than one order of magnitude existing between the melt-quenched ($p_H \sim 2\times10^{21}$ cm^{-3}) and slowly-cooled ($p_H \sim 10^{20}$ cm^{-3}) samples. Slightly increasing x to 0.03 has a spectacular impact on p_H that decreases to 8×10^{19} cm^{-3} at 300 K for the x = 0.03 melt-quenched sample. As shown in Figures 3c and 3d, the reduction in p_H with x has also a significant influence on the hole mobility μ_H which strongly increases with x. At temperatures below 30 K, μ_H is constant for all samples suggestive of hole scattering by neutral impurities. Between 50 and 300 K, μ_H follows approximately a $T^{-0.25}$ law for x = 0 while μ_H varies more strongly with temperature for the other samples following a temperature dependence close to $\mu_H \sim T^{-1/2}$.

Consistent with the metallic nature of these samples, the α values are moderate near room temperature (Figures 4a and 4b) and decrease from 30 to 15 μV K^{-1} at 300 K when x varies from 0 to 0.03 for both series. Due to the highly-degenerate character of transport in these compounds, a linear temperature dependence may be expected along with α values that decrease with increasing p_H. However, neither of these expectations are observed in the present case with all samples exhibiting strong deviations from linearity. Furthermore, the α values do not trend with the hole concentration, the x = 0.03 melt-quenched sample showing concomitantly the lowest α and p_H values. Of note, the very low α values observed in the x = 0.03 samples result in significantly lower ZT values than those obtained in the slowly-cooled and melt-quenched x = 0.0 samples (Figure S2 in Supplemental Material, Ref. 42). However, this trend reverses at temperatures higher than 300 K due to the contribution of the second heavy-hole valence band.

In addition to governing the electronic transport, the introduction of excess Sn also significantly influences the thermal transport, as shown in Figures 5a and 5b. The main difference between the different samples is observed below 100 K where the magnitude of the Umklapp peak, typical of crystalline compounds, clearly increases with increasing *x*. This trend is consistent with Sn vacancies acting as efficient point defect scatterers. Below 10 K, $\kappa(T)$ follows approximately a $T^{3/2}$ law suggesting that the phonon relaxation time still depends on temperature.

Discussion

Sensitivity of the hole concentration to the synthetic conditions

Our results evidence the strong sensitivity of the transport properties of $Sn_{1+x}Te$ to the synthetic conditions employed which dictate the final concentration of Sn vacancies in the samples. The actual concentration of Sn vacancies $[V_{Sn}]$ can be estimated if we assume that each vacancy acts as a double acceptor and that the Hall factor r_H is close to unity. In such a case, $[V_{Sn}]$ is simply equal to $p_H/2$ and can be further expressed as $[V_{Sn}] = S\delta$, with S = 1.58×10^{22} cm^{-3} the number of Sn sites in the crystal lattice. Taking these two hypotheses as valid, an estimation of the actual Sn content (expressed as δ in $Sn_{1-\delta}Te$) is given in Table 1. Brebrick *et al.*[50] have established a relation that relates the percentage of Te, y, in the chemical formula to the lattice parameter $a = 6.3278 - 3.54(y - 0.5)$. With $y = 1/(2 - \delta)$, the theoretical lattice parameters can be thus compared to the experimental values inferred from Rietveld refinements. As shown in Table 1, a very good agreement between theory and experiment is obtained for samples with hole concentrations below 10^{20} cm^{-3} indicating that the above-mentioned assumptions are reasonable. However, clear differences emerge for samples

exhibiting hole concentrations above 3×10^{20} cm^{-3}, the discrepancy being even more pronounced as the hole concentration further increases. The breakdown of this simple approach is a signature of the second, heavy-hole valence band whose contribution to transport cannot be neglected at very high hole concentrations. In this regime, significant deviations of r_H from unity are mainly responsible for this discrepancy, as suggested in early reports indicating that r_H can deviate from unity by up to 40%, that is, fall in the range of 0.6 – 0.9.[29,30] Alternatively, estimates of the Sn content in these samples can be obtained by using instead the experimental lattice parameters yielding δ values of 0.66% and 1.76% for the $Sn_{1-\delta}Te$ samples prepared by slow cooling and melt-quenching, respectively.

The strong sensitivity of the vacancy concentration to the synthetic conditions is a consequence of the high vapor pressure of both SnTe and Te_2 above the congruent melting point at 806°C.[41,51] The partial pressures of gaseous SnTe and Te_2 are on the same order of magnitude above this temperature (1 and 0.4 mbar, respectively, around 800°C) leading to a loss of both elements during the synthetic process and, eventually, to variations in the concentration of Sn vacancies in the final composition. Because the melt-spinning process is performed in an open silica tube, the sublimation also explains why the sample prepared by this technique exhibits a hole concentration equivalent to that of the $Sn_{1.03}Te$ sample prepared by melt-quenching.

In addition to the synthetic conditions employed, excess Sn also acts as an efficient parameter to adjust the vacancy concentration. Our TEM and Mössbauer investigations nevertheless show that the introduction of excess Sn does not lead to an enhancement in the solubility of Sn into the unit cell of SnTe. Considering the Sn-rich and Te-rich solidus lines in the Sn-Te phase diagram, the excess Sn shifts the path followed upon cooling towards the Sn-rich side and, meanwhile, lessens the impact of sublimation at high temperatures. These combined effects help to maintain a chemical composition close to the lowest Te concentration of 50.1at% resulting in the lowest hole concentrations.

Scattering mechanism and Ioffe-Pisarenko plot

One important general finding evidenced by our results is the temperature dependence of the Hall mobility μ_H. Below 20 K, all samples exhibit constant μ_H values suggesting neutral impurity scattering as the main source of hole diffusion. Above this temperature, $\mu_H(T)$ follows a power law T^{-r} with an exponent r close to 0.5, except for the sample with the highest p_H (1.1×10^{21} cm^{-3} at 300 K) where an exponent of 0.25 is observed. r barely varies with p_H over nearly an order of magnitude between 7×10^{19} cm^{-3} and 4×10^{20} cm^{-3} at 300 K and is insensitive to the synthetic conditions used. Both variations significantly deviate from the T^{-1} law expected for acoustic phonon scattering in degenerate semiconductors with non-parabolic bands.[52] The r value inferred is closer to the $T^{-0.5}$ dependence characteristic of alloy scattering and usually observed in solid solutions or in strongly disordered compounds.[53-56] The robustness of the r value indicates that μ_H in $Sn_{1+x}Te$ is mainly limited by the level of disorder induced by the Sn vacancy concentration. Noteworthy, as we shall see below, the alloy scattering and acoustic phonon relaxation times exhibit similar energy and density-of-states effective mass dependences, which explains why assuming acoustic phonon scattering provides an adequate description of the transport data in SnTe-based compounds.

Another interesting question is whether the deviations of r from unity could be due to either temperature-dependent density-of-states effective masses m^* as observed in lead chalcogenides or, alternatively, to the presence of other scattering mechanisms. The first possibility cannot account for a decrease in r since, in lead chalcogenides, the temperature dependence of $m^* \sim T^{0.4}$ combines with the temperature dependence of the relaxation time ($\tau \sim T^{-3/2}m^{*-3/2}$ and $\tau \sim T^{-1}m^{*-2}$ for non-degenerate and degenerate semiconductors, respectively, both with acoustic phonon scattering),[52] systematically giving rise to an increase in the exponent value r ($\mu \sim \tau/m^*$). The possible presence of other scattering mechanisms such

as ionized impurity, polar optical phonon, interband and electron-electron scattering, which have all been discussed in lead chalcogenides,[52] is restrained by available experimental data on SnTe and PbTe. Ionized impurity is strongly lessened in SnTe due to its high dielectric constant (~1700).[56] Although the partial ionicity of the chemical bonding and the very low Debye temperature (~140 K) of SnTe suggests that polar optical phonons may also play a role in the scattering mechanisms below 300 K, this mechanism yields a temperature dependence of $\mu_H \propto T^{-1}$ in degenerate semiconductors with non-parabolic bands, that is, similar to that expected for acoustic phonon scattering.[52] The presence of the two valence bands in SnTe raises the question of interband scattering between the two inequivalent band maxima. A comparison with PbTe and PbTe-SnTe alloys indicates, however, that this mechanism is expected to become important only at high temperatures (typically above 400 K) where the energy offset between the two bands is significantly lowered.[52] Finally, electron-electron scattering has been shown to lower the exponent value r in PbTe to values ranging between 0 and 0.3.[52] In such a case, a single relaxation time can no longer be defined for all the mechanisms due to the inelastic nature of these collisions. Since this effect occurs in samples with carrier concentrations higher than 2×10^{18} cm^{-3}, that is, an order of magnitude lower than the hole concentrations measured in $Sn_{1+x}Te$, a possible contribution of these inelastic processes cannot be strictly ruled out in the present case.

We further tried to model the variations in μ_H with p_H using expressions of the relaxation times for acoustic phonon and polar optical scattering and taking into account the non-parabolic character of the light-hole valence band (see equations in Supplemental Material, Ref. 42). The results of these calculations, plotted in Figure 6, first confirm that polar optical scattering does not significantly modify μ_H in the hole concentration range covered. In contrast to PbX (X = S, Se and Te) compounds, p_H in $Sn_{1+x}Te$ is too high to reach a regime where polar scattering would affect noticeably the carrier relaxation time. While most of the parameters used in this model

have been derived from experimental data or theoretical calculations, the deformation potential Ξ remains less well documented in SnTe compared to PbX.[49] This parameter, which determines the degree of coupling between acoustic phonons and charge carriers, has been determined only for few semiconductors and usually ranges between 8 and 35 eV.[58] In lead chalcogenides, Ξ was found to vary between 20 eV in PbS up to 35 eV in *p*-type PbSe.[59] For SnTe, only the optical deformation potential D_{iso} = – 8.68 eV has been evaluated theoretically by subtracting the isotropic deformation potential of the valence band from that of the conduction band (the negative value is due to the band inversion at the L point of the Brillouin zone).[60] Assuming solely acoustic phonon scattering, the variation of μ_H with p_H can be consistently explained at 300 K with a Ξ value of 12.5 eV (see Figure 6). However, because the alloy scattering and acoustic phonon relaxation times vary similarly as a function of energy, their relative importance cannot be determined by this model. This drawback is due to the fact that, while alloy scattering is fixed at a given temperature and hole concentration, p_H should remain constant in order to clearly disentangle the roles of these scattering mechanisms on μ_H. Moreover, the alloy scattering potential U, which determines the magnitude of the reduction in μ_H for a given chemical composition, is unknown for SnTe-based systems.

The non-trivial evolution of the thermopower as a function of both temperature and p_H is another interesting finding evidenced by these results. The highly-degenerate character of these samples should result in a linear increase in α with temperature so long as the temperature dependence of the density-of-states effective mass is negligible. In contrast to this simple expectation, significant deviations from linearity emerges below 100 K. In lead chalcogenides, the density-of-states effective mass has been shown to be practically temperature-independent below this temperature.[52] The strong similarities between these materials and SnTe suggest that such variation does not provide a consistent explanation for this low-temperature behavior. Furthermore, the shape of the $\alpha(T)$ curves below 100 K is strongly sensitive to the synthetic

conditions used or, equivalently, to p_H. This is further confirmed by measurements performed on a x = 0.01 sample synthesized by melt-quenching which shows a distinct p_H value and $\alpha(T)$ curve (see Figure S3 in Supplemental Material, Ref. 42). Several possible explanations may be considered to understand these variations in T and p_H, that is, modifications in the electronic band structure, variations in the scattering mechanism or a phonon drag contribution.

Intuitively, it seems unlikely that the very small variations in the Sn vacancy concentration between the different samples can alter significantly the valence band structure beyond a rigid shift of the chemical potential. A change in the energy dependence of the scattering mechanism could in principle induce a variation in α. Both quantities are related via the scattering exponent defined generally by $r = \partial \ln[\tau(\varepsilon)]/\partial \ln(\varepsilon)$ where $\tau(\varepsilon)$ is the relaxation time, ε is the energy. For a degenerate semiconductor with non-parabolic bands, α depends on r via the expression $\alpha = \frac{\pi^2}{3}\frac{k_B^2}{e}\frac{T}{\epsilon_F}\left(r + \frac{3}{2} - \frac{\frac{2\epsilon_F}{\epsilon_g}}{1+\frac{2\epsilon_F}{\epsilon_g}} + \frac{3}{2}\frac{\frac{\epsilon_F}{\epsilon_g}}{1+\frac{\epsilon_F}{\epsilon_g}}\right)$ where k_B is the Boltzmann constant, e is the elementary charge, ϵ_F is the Fermi level and ϵ_g is the band gap.[52] While an increase in r with T would yield an additional T dependence giving rise to deviations of $\alpha(T)$ from a diffusive regime for which $\alpha \propto T^1$, the μ_H data do not show differences from sample to sample and thus, does not make such variations in r a viable explanation in the present case.

A consistent mechanism explaining the observed trend is rather provided by a phonon-drag contribution besides the diffusion thermopower. The strongest effect is observed in samples which exhibit the lowest hole concentrations with a maximum in α of about 10 μV.K^{-1} near 50 K. Upon increasing p_H to 10^{21} cm^{-3}, this maximum is still clearly discernable but strongly lessened. This behavior can be explained by considering that, at low p_H values, electron-phonon interactions that give rise to the phonon-drag effect are favored compared to phonon-alloy scattering due to the very low amount of Sn vacancies. As p_H increases to higher values, phonon-alloy scattering competes with electron-phonon interactions which modifies the

phonon-drag contribution. In addition, it was shown in lead chalcogenides that, at high charge carrier concentrations, phonons exert less drag due to the influence of phonon scattering off free charge carriers resulting in a lower contribution to the thermopower.[52] This fact is consistent with the lower maximum in α observed for the melt-quenched SnTe sample which shows the highest hole concentration. The overall behavior of α in $Sn_{1+x}Te$ samples is thus qualitatively similar to what has been observed in PbTe-based compounds with a phonon-drag contribution superimposed to the diffusion thermopower whose magnitude sensitively depends on the chemical composition.[61]

The $\alpha(T)$ data also provide another experimental evidence that band parameters depend on temperature as those in lead chalcogenides do. Above 200 K, most of the samples experience a steeper rise in α which is more clearly visualized when the high-temperature data are added (see Figure S4 in Supplemental Material, Ref. 42). This stronger-than-linear increase in temperature is likely a direct signature of the temperature dependence of the density-of-states effective masses, determined between 300 and 800 K,[14] that extends to temperatures below 300 K.

The thermopower and Hall effect data measured at 300 K can be combined and compared to the Ioffe-Pisarenko curve calculated by a two-valence-band model which predicts the hole concentration dependence of the thermopower.[12,29,30] The theoretical curve, shown as a solid black line in Figure 7, has been calculated considering a two-valence band model with acoustic phonon scattering, first developed by Brebrick *et al.*[29,30] The experimental data are well described by the theoretical curve for hole concentrations ranging between 3×10^{20} cm^{-3} up to 1.2×10^{21} cm^{-3}, that is, in a region dominated by the parabolic, heavy-hole valence band. For hole concentrations lower than 3×10^{20} cm^{-3}, some deviations between theory and experiment can be observed with the experimental points being systematically above the predicted values. Since this region is dominated by the non-parabolic, light-hole valence band, the density-of-

states effective mass depends on the hole concentration. Because a single, average value is used to calculate this theoretical curve, this may explain the slight difference observed in this region.

Lorenz number and lattice thermal conductivity

The low ρ values measured in all the samples give rise to a large electronic contribution to the thermal conductivity $\kappa_e = LT/\rho$. In order to disentangle the electronic and the lattice contributions, an estimate of the Lorenz number L needs to be obtained. In principle, the two-band model used to generate the Ioffe-Pisarenko plot may be used to determine the Lorenz numbers. However, this approach, applicable to the $Sn_{1+x}Te$ samples with the lowest hole concentrations, cannot be extended to the samples with the highest hole concentration at 300 K. For this sample, the calculated Lorenz numbers are close to the degenerate limit leading to overestimated κ_e and hence, to unphysical κ_L values. This breakdown is the result of the presence of the two valence bands which tend to decrease the Lorenz numbers despite the degenerate behavior of the samples. Recent theoretical studies have indeed shown that the presence of multiple bands acts as an energy filter that contributes to lower L despite the degenerate nature of the charge carrier gas.[62,63] This effect cannot be adequately captured by transport models and thus, gives rise to difficulties in estimating correctly the lattice thermal conductivity, especially above 300 K where L is strongly temperature-dependent.

At low temperatures, these inherent difficulties can be partially circumvented by considering a simple single-parabolic band model with acoustic phonon scattering.[7-28] This approach has been shown to yield reasonable κ_L values in SnTe despite its strict applicability is questionable. Adopting this approach, the results show that the variations in the concentration of Sn vacancies with the synthesis process employed has also a significant impact on κ_L (Figure 8). The main effect is tied to a strong reduction in the Umklapp peak at low temperatures

evidencing a clear trend between the amount of Sn vacancies estimated from the Hall data and the magnitude of the peak. The samples that exhibit the lowest hole concentrations and hence, the lowest concentration of Sn vacancies, exhibit the highest Umklapp peak that reaches 16 W m^{-1} K^{-1} near 30 K. These results indicate that Sn vacancies act as a significant source of point defect scattering at low temperatures. This conclusion is further corroborated by a fit of the experimental data using the Debye-Callaway model.[64] In this model, the phonon relaxation time was assumed to be the sum of three independent terms that describe grain boundary scattering, point-defect scattering and phonon-phonon Umklapp scattering (see equations in Supplemental Material, Ref. 42). As shown in Figure 8, this simple model describes very well the experimental results. In addition to yielding an average grain size on the order of few microns, these fits show that the *A* parameter, related to point defect scattering, decreases by one order of magnitude with increasing the Sn excess (Table 2). The parameter *A* is expected to scale as $x(1-x)$ where x is the concentration of point defects in the sample. Assuming $x = \delta$ in the present case (see Table 1 for the δ values; for the slowly-cooled and melt-quenched SnTe samples, the estimates of δ obtained from the experimental lattice parameters have been used) indeed results in a quasi linear correlation between *A* and $\delta(1-\delta)$, as shown in Figure 9.

Finally, the evolution observed in κ_L at low temperatures reinforces the scenario of a phonon-drag effect which also depends on the low-temperature phonon mean free path l_{ph}. Because large l_{ph} values will favor a significant phonon-drag contribution, high vacancy concentrations, which tend to decrease l_{ph}, will strongly limit the phonon-drag effect. Thus, the interplay between the amount of vacancies, the lattice thermal conductivity and the phonon-drag effect provides a consistent framework to explain the low-temperature transport data in these samples.

Summary and Conclusion

In summary, the transport properties of polycrystalline $Sn_{1+x}Te$ ($0 \leq x \leq 0.03$) have been measured down to liquid helium temperatures to determine the influence of the synthetic route employed. The different synthesis methods lead to strong variations in the hole concentration controlled by the Sn vacancy concentration. Samples prepared with excess Sn systematically show elemental Sn located at the grain boundaries. Transport properties measurements have further highlighted the complexity of the transport in $Sn_{1+x}Te$ arising from the multiband nature of the valence band structure and various physical phenomena responding to variations in temperature and hole concentration. The robustness of the exponent describing the temperature dependence of the Hall mobility, the strongly non-linear temperature dependence of the thermopower due to a phonon-drag contribution and the apparent significant deviations of the Lorenz number from the degenerate limit are all important experimental manifestations of the complexity of the transport in SnTe. These results call for further investigations in order to fully determine the role played by the heavy valence bands at high hole concentrations on the low-temperature electronic and phonon transport in $Sn_{1+x}Te$. In addition, our findings provide a good basis for better understanding the role played by substituting elements on the transport properties of this important chalcogenide compound.

Acknowledgment

The authors thank the financial support of the European Space Agency under NPI contract N°40001134346/15/NL/RA and of the Région Lorraine.

References

[1] Goldsmid, H. J. in *Thermoelectric Refrigeration*; Springer: New York, 1964.

[2] *Thermoelectrics and its Energy Harvesting*, edited by D. M. Rowe (CRC Press, 2012).

[3] H. Wang, A. LaLonde, Y. Pei, G. J. Snyder, Adv. Funct. Mater. **23**, 1586 (2013).

[4] Y. Pei, H. Wang, G. J. Snyder, Adv. Mater. **24**, 6125 (2012).

[5] Y. Lee, S.-H. Lo, J. Androulakis, C.-I. Wu, L.-D. Zhao, D.-Y. Chung, T. P. Hogan, V. P. Dravid and M. G. Kanatzidis, J. Am. Chem. Soc. **135**, 5152 (2013).

[6] J. P. Heremans, V. Jovovic, E. S. Toberer, A. Saramat, K. Kurosaki, A. Charoenphakdee, S. Yamanaka and G. J. Snyder, Science **321**, 554 (2008).

[7] G. Tan, L-D. Zhao, F. Shi, J. W. Doak, S.-H. Lo, H. Sun, P. Wang, C. Wolverton, V. P. Dravid, C. Uher, and M. G. Kanatzidis, J. Am. Chem. Soc. **136**, 7006 (2014).

[8] G. Tan, F. Shi, J. W. Doak, H. Sun, L-D. Zhao, P. Wang, C. Uher, C. Wolverton, V. P. Dravid and M. G. Kanatzidis, Energy Environ. Sci. **8**, 267 (2015).

[9] G. Tan, F. Shi, S. Hao, H. Chi, T. P. Bailey, L-D. Zhao, C. Uher, C. Wolverton, V. P. Dravid, and M. G. Kanatzidis, J. Am. Chem. Soc. **137**, 11507 (2015).

[10] G. Tan, F. Shi, S. Hao, H. Chi, L-D. Zhao, C. Uher, C. Wolverton, V. P. Dravid, and M. G. Kanatzidis, J. Am. Chem. Soc. **137**, 5100 (2015).

[11] G. Tan, W. G. Zeier, F. Shi, P. Wang, G. J. Snyder, V. P. Dravid, and M. G. Kanatzidis, Chem. Mater. **27**, 7801 (2015).

[12] Q. Zhang, B. Liao, Y. Lan, K. Lukas, W. Liu, K. Esfarjani, C. Opeil, D. Broido, G. Chen and Z. Ren, Proc. Antl. Acad. Sci. USA **110**, 13261 (2013).

[13] J. He, X. Tan, J. Xu, G.-Q. Liu, H. Shao, Y. Fu, X. Wang, Z. Liu, J. Xu, H. Jiang and J. Jiang, J. Mater. Chem. A **3**, 19974 (2015).

[14] M. Zhou, Z. M. Gibbs, H. Wang, Y. Han, C. Xin, L. Li and G. J. Snyder, Phys. Chem. Chem.

Phys. **16**, 20741 (2014).

[15] A. Banik, U. S. Shenoy, S. Anand, U. W. Waghmare and K. Biswas, Chem. Mater. **27**, 581 (2015).

[16] A. Banik, B. Vishal, S. Perumal, R. Datta and K. Biswas, Energy Environ. Sci. **9**, 2011 (2016).

[17] R. Al Rahal Al Orabi, N. A. Mecholsky, J. Hwang, W. Kim, J.-S. Rhyee, D. Wee and M. Fornari, Chem. Mater. **28**, 376 (2016).

[18] R. Al Rahal Al Orabi, J. Hwang, C.-C. Lin, R. Gautier, B. Fontaine, W. Kim, J.-S. Rhyee, D. Wee and M. Fornari, Chem. Mater. **29**, 612 (2017).

[19] L. Zhang, J. Wang, Z. Cheng, Q. Sun, Z. Li and S. Dou, J. Mater. Chem. A **4**, 7936 (2016).

[20] Z. Zhou, J. Yang, Q. Jiang, Y. Luo, D. Zhang, Y. Ren, X. He and J. Xin, J. Mater. Chem. A **4**, 13171 (2016).

[21] L-D. Zhao, X. Zhang, H. Wu, G. Tan, Y. Pei, Y. Xiao, C. Chang, D. Wu, H. Chi, L. Zheng, S. Gong, C. Uher, J. He and M. G. Kanatzidis, J. Am. Chem. Soc. **138**, 2366 (2016).

[22] S. Roychowdhury, U. S. Shenoy, U. V. Waghmare and K. Biswas, J. Mater. Chem. C **5**, 5737 (2017).

[23] W. Li, L. Zheng, B. Ge, S. Lin, X. Zhang, Z. Chen, Y. Chang and Y. Pei, Adv. Mater. **29**, 1605887 (2017).

[24] L. Wang, X. Tan, G. Liu, J. Xu, H. Shao, B. Yu, H. Jiang, S. Yue and J. Jiang, ACS Energy Lett. **2**, 1203 (2017).

[25] L. Zheng, W. Li, S. Lin, J. Li, Z. Chen and Y. Pei, ACS Energy Lett. **2**, 563 (2017).

[26] L. Hu, Y. Zhang, H. Wu, J. Li, Y. Li, M. McKenna, J. He, F. Liu, S. J. Pennycook, X. Zeng, Adv. Energy Mater. **8**, 1802116 (2018).

[27] N. Wang, D. West, J. Liu, J. Li, Q. Yan, B.-L. Gu, S. B. Zhang, W. Duan, Phys. Rev. B **89**, 045142 (2014).

[28] J. Q. Li, S. Huang, Z. P. Chen, Y. Li, S. H. Song, F. S. Liu, W. Q. Ao, Phys. Chem. Chem. Phys. **19**, 28749 (2017).

[29] R. F. Brebrick and A. J. Strauss, Phys. Rev. **131**, 104 (1963).

[30] R. F. Brebrick, J. Phys. Chem. Solids **24**, 27 (1963).

[31] J. A. Kafalas, R. F. Brebrick and A. J. Strauss, Appl. Phys. Lett. **4**, 93 (1964).

[32] D. M. Chigikov and V. P. Schastliviy in *Tellure and Tellurides* (Moscow, Nauka, 1966, in Russian).

[33] L. M. Rogers, J. Phys. D: Appl. Phys. **1**, 845 (1968).

[34] D. J. Singh, Funct. Mater. Lett. **3**, 223 (2010).

[35] Y. Tanaka, Z. Ren, T. Sato, K. Nakayama, S. Souma, T. Takahashi, K. Segawa and Y. Ando, Nat. Phys. **8**, 800 (2012).

[36] D. Ibrahim, V. Ohorodniichuk, C. Candolfi, C. Semprimoschnig, A. Dauscher, B. Lenoir, ACS Omega **2**, 7106 (2017).

[37] J. Rodriguez-Carvajal, Physica B **192**, 55 (1993).

[38] L. E. Shelimova and N. K. Abrikosov, Russ J Inorg Chem **9**, 1017 (1964).

[39] L. E. Glukhikh and N. K. Abrikosov, Russ J Inorg Chem **8**, 930 (1963).

[40] R. F. Brebrick, J. Electron. Mater. **6**, 659 (1977).

[41] R. F. Brebrick and A. J. Strauss, J. Chem. Phys. **41**, 197 (1964).

[42] See Supplemental Material at (URL) for additional HRTEM images, detailed analysis of the Mössbauer data, additional transport properties measurements and equations used to model the hole concentration dependence of the hole mobility and the temperature dependence of the lattice thermal conductivity.

[43] W. Keune, Phys. Rev. **10**, 5057 (1974).

[44] V. A. Bruykhanov, N. N. Delyagin, R. N. Kuz'min and V. S. Shpinel, Sov. Phys. –JETP **19**, 1344 (1964).

[45] R. D. Taylor and P. P. Craig, Phys. Rev. **175**, 782 (1968).

[46] O. Valassiades and N. A. Economou, Phys. Status Solidi A **30**, 187 (1975).

[47] P. B. Littlewood, B. Mihaila, R. K. Schulze, D. J. Safarik, J. E. Gubernatis, A. Bostwick, E. Rotenberg, C. P. Opeil, T. Durakiewicz, J. L. Smith, J. C. Lashley, Phys. Rev. Lett. **105**, 086404 (2010).

[48] C. D. O'Neill, D. A. Sokolov, A. Hermann, A. Bossak, C. Stock, and A. D. Huxley, Phys. Rev. B **95**, 144101 (2017).

[49] K. L. I. Kobayashi, Y. Kato, Y. Katayama, and K. F. Komatsubara, Phys. Rev. Lett. **37**, 772 (1976).

[50] R. F. Brebrick, J. Phys. Chem. Solids, **32**, 551 (1971).

[51] Y. Huang and R. F. Brebrick, J. Electrochem. Soc. **135**, 1547 (1988).

[52] Y. I. Ravich, *Semiconducting Lead Chalcogenides* (Plenum Press, New York, NY, 1979), and references therein.

[53] L. Makowski, M. Glicksman, J. Phys. Chem. Solids **34**, 487 (1973).

[54] V. W. L. Chin, R. J. Egan, T. L. Tansley, J. Appl. Phys. **69**, 3571 (1991).

[55] J. W. Harrison, J. R. Hauser, Phys. Rev. B **13**, 5347 (1976).

[56] J. R. Hauser, M. A. Littlejohn, T. H. Glisson, Appl. Phys. Lett. **28**, 458 (1976).

[57] G. Nimtz and B. Schlicht, *Narrow-Gap Semiconductors* (Berlin Heidelberg: Springer-Verlag, 1983).

[58] Springer Materials, Landolt-Börnstein Database. Available at www.springermaterials.com.

[59] H. Weng, Y. Pei, A. D. LaLonde and G. J. Snyder, Proc. Nat. Acad. Sci. **109**, 9705 (2012).

[60] S. Rabii, Phys. Rev. **182**, 821 (1969).

[61] C. M. Jaworski, M. D. Nielsen, H. Wang, S. N. Girard, W. Cai, W. D. Porter, M. G. Kanatzidis, J. P. Heremans, Phys. Rev. B **87**, 045203 (2013).

[62] R. W. McKinney, P. Gorai, V. Stevanovic, E. S. Toberer, J. Mater. Chem. A **5**, 17302 (2017).

[63] M. Thesberg, H. Kosina, N. Neophytou, Phys. Rev. B **95**, 125206 (2017).

[64] J. Callaway, Phys. Rev. **113**, 1046 (1959).

Tables

Table 1. Theoretical Sn vacancy concentration δ in the $Sn_{1-\delta}Te$ samples prepared by melt-spinning (MS), melt-quenching (MQ) and slow cooling (SC). The corresponding Te content and theoretical lattice parameters a_{th} are also given. The experimental lattice parameters a_{exp} have been inferred from Rietveld refinements against the PXRD data obtained on powdered samples. The different samples have been sorted out according to the hole concentration p_H measured by Hall effect. Note that using the a_{exp} values, estimates of δ of 0.0066 and 0.0176 are obtained for the SnTe SC and MQ samples, respectively.

Sample	p_H (cm^{-3})	δ ($Sn_{1-\delta}Te$)	Composition	at. %Te	a_{th} (Å)	a_{exp} (Å)
SnTe MS	7.3×10^{19}	0.0023	$Sn_{0.9977}Te$	50.06	6.3258	6.3240
$Sn_{1.03}Te$ MQ	8.0×10^{19}	0.0025	$Sn_{0.9975}Te$	50.06	6.3258	6.3242
$Sn_{1.03}Te$ SC	1.2×10^{20}	0.0038	$Sn_{0.9962}Te$	50.10	6.3244	6.3231
SnTe SC	3.3×10^{20}	0.0104	$Sn_{0.9896}Te$	50.26	6.3185	6.3219
SnTe MQ	1.1×10^{21}	0.0348	$Sn_{0.9652}Te$	50.90	6.2964	6.3120

Table 2. Values of the parameters *L*, *A* and *B* determined by fits of the low-temperature lattice thermal conductivity data of the $Sn_{1+x}Te$ samples to the Debye-Callaway model. The letters MQ, SC and MS refers to the preparation process (melt-quenched, slow-cooling and melt-spinning, respectively).

Echantillon	*L* (μm)	*A* (10^{-42} s^3)	*B* (10^{-18} $s.K^{-1}$)
SnTe (MQ)	1.5	42	1.3
$Sn_{1.03}Te$ (MQ)	1.3	5	6.0
SnTe (SC)	1.0	18	3.0
$Sn_{1.03}Te$ (SC)	1.1	8	4.6
SnTe (MS)	1.4	4.6	6.6

Figure Captions

Figure 1. a) STEM images of quenched $Sn_{1.03}Te$ taken along the [100] direction. The corresponding maps for Sn (red) and Te (green) are also shown. The last image is an overlaid of the Sn and Te maps. For all panels, the white bar corresponds to 200 nm. **b)** (left panel) ^{119}Sn Mössbauer spectrum at 4.2 K of $Sn_{1.03}Te$ prepared by melt-quenching. The experimental data points are shown in black while the red curve represents the least-squares fit. Spectral components due to Sn^{2+}, Sn^{0} and Sn^{4+} are shown by the dashed, dashed-dotted and dotted lines, respectively. The peak observed with an isomer shift close to zero is due to a minute amount of SnO_2. The isomer shift of the main peak (IS = 3.56 mm s^{-1}) is consistent with a Sn^{2+} oxidation state in SnTe. (right panel) Sharpened spectrum obtained with the following parameters (see Supplemental Material for the detailed procedure, Ref. 42) N = 400, V_1 = – 8 mm/s, V_2 = 8 mm/s, Γ = 0.70 $mm.s^{-1}$. The black arrows indicate the Sn^{0} peak positions characterizing its doublet.

Figure 2. Comparison of the temperature dependences of the electrical resistivity ρ of (a) SnTe and (b) $Sn_{1.03}Te$ samples prepared by melt-quenching (MQ), slow-cooling (SC) and melt-spinning (MS).

Figure 3. Temperature dependences of the hole concentration p_H (panels a and b) and Hall mobility μ_H (panels c and d) of the SnTe and $Sn_{1.03}Te$ samples prepared by melt-quenching (MQ), slow-cooling (SC) and melt-spinning (MS).

Figure 4. Comparison of the temperature dependence of the thermopower α of (a) SnTe and (b) $Sn_{1.03}Te$ samples prepared by melt-quenching (MQ), slow-cooling (SC) and melt-spinning (MS).

Figure 5. Total thermal conductivity κ as a function of temperature for the (a) SnTe and (b) $Sn_{1.03}Te$ samples prepared by melt-quenching (MQ), slow-cooling (SC) and melt-spinning (MS).

Figure 6. Hall mobility μ_H as a function of the hole density p_H measured at 300 K (red symbols). The green dotted curve has been calculated assuming only acoustic phonon scattering (*ac*) while the blue solid curve has been obtained by combining acoustic phonon scattering and polar optical phonon scattering (*ac* + *po*). The deformation potential Ξ, the main parameter that determines the μ_H values for acoustic phonon scattering, has been adjusted to match the experimental data yielding a value of 12.5 eV.

Figure 7. Thermopower α as a function of the hole concentration p_H at 300 K. The solid black curve has been generated by a two-non-degenerate-valence-band model with acoustic phonon scattering. In the legend, the letters MQ, SC and MS refers to the preparation process used (melt-quenching, slow cooling and melt-spinning, respectively).

Figure 8. Lattice thermal conductivity as a function of temperature of the (a) SnTe and (b) $Sn_{1.03}Te$ samples prepared by melt-quenching (MQ), slow-cooling (SC) and melt-spinning (MS). The solid black curves are numerical fitting results of the Debye-Callaway model.

Figure 9. Parameter A inferred from fits of the lattice thermal conductivity to the Debye-Callaway model as a function of $\delta(1-\delta)$ where δ corresponds to the estimated concentration of Sn vacancies. The solid black line stands for the best linear fit to the data. For the slowly-cooled and melt-quenched samples, estimates of δ of 0.0066 and 0.0176 have been considered.

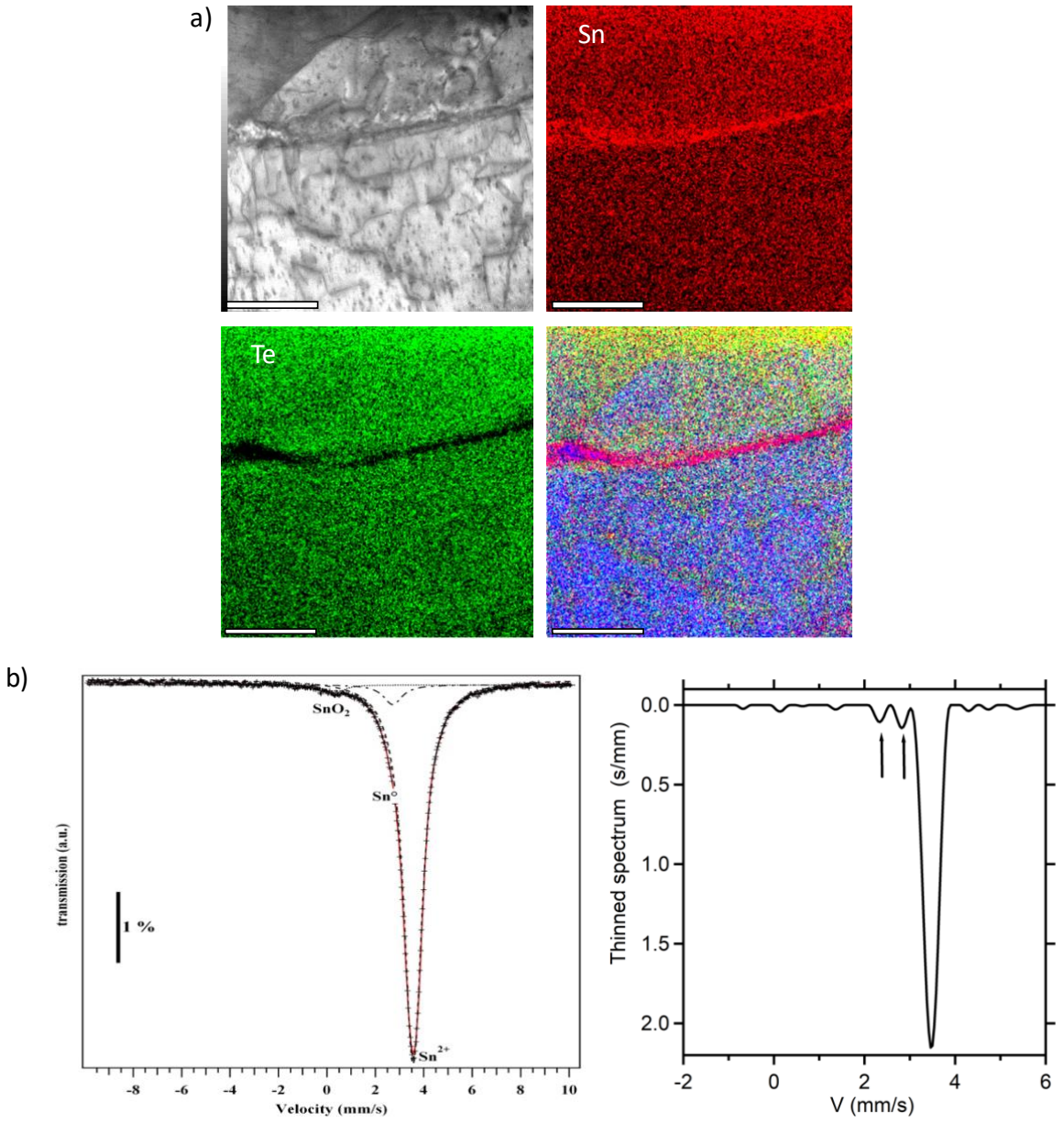

Figure 1

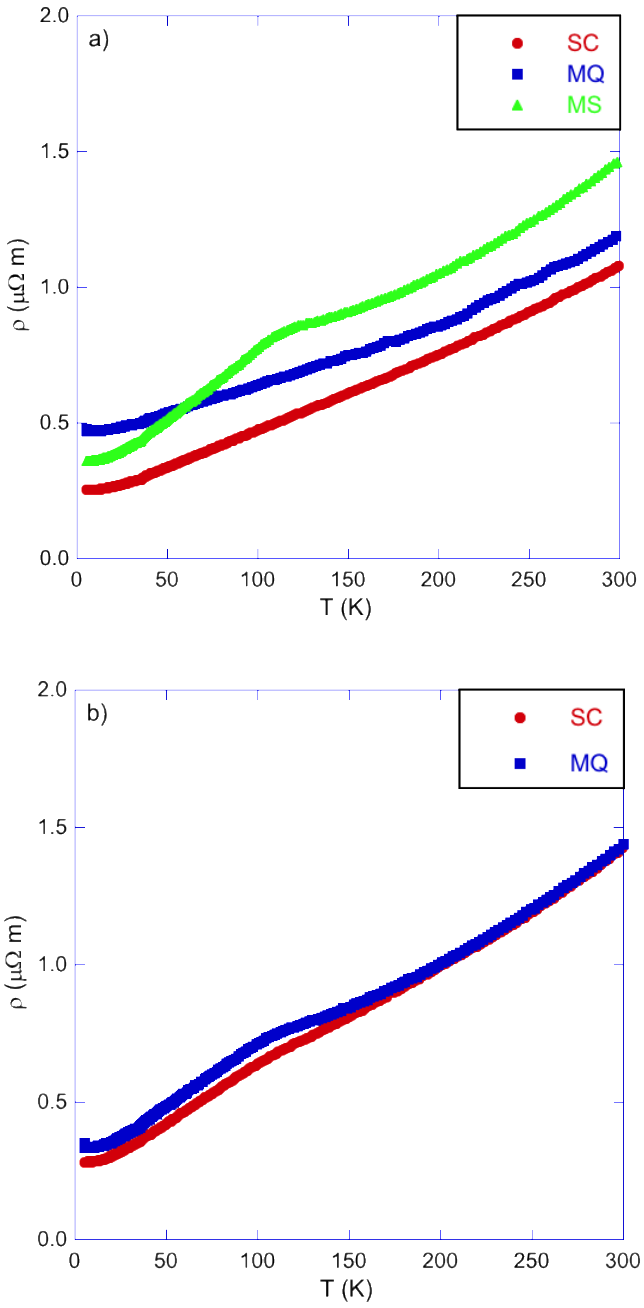

Figure 2

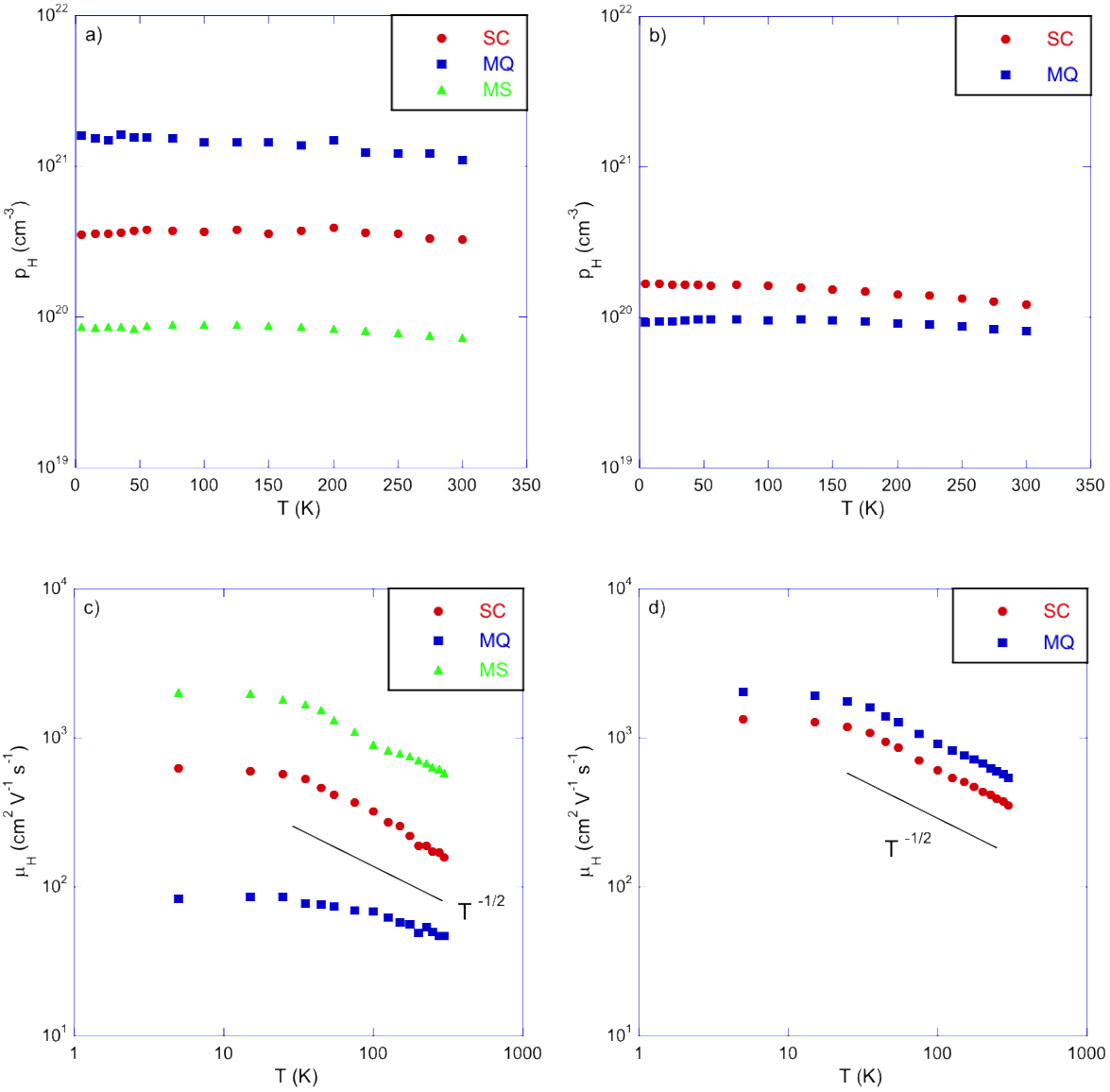
a)
SC
MQ
MS
p_H (cm^{-3})
T (K)
b)
SC
MQ
p_H (cm^{-3})
T (K)
c)
SC
MQ
MS
μ_H ($cm^2 V^{-1} s^{-1}$)
$T^{-1/2}$
T (K)
d)
SC
MQ
μ_H ($cm^2 V^{-1} s^{-1}$)
$T^{-1/2}$
T (K)

Figure 3

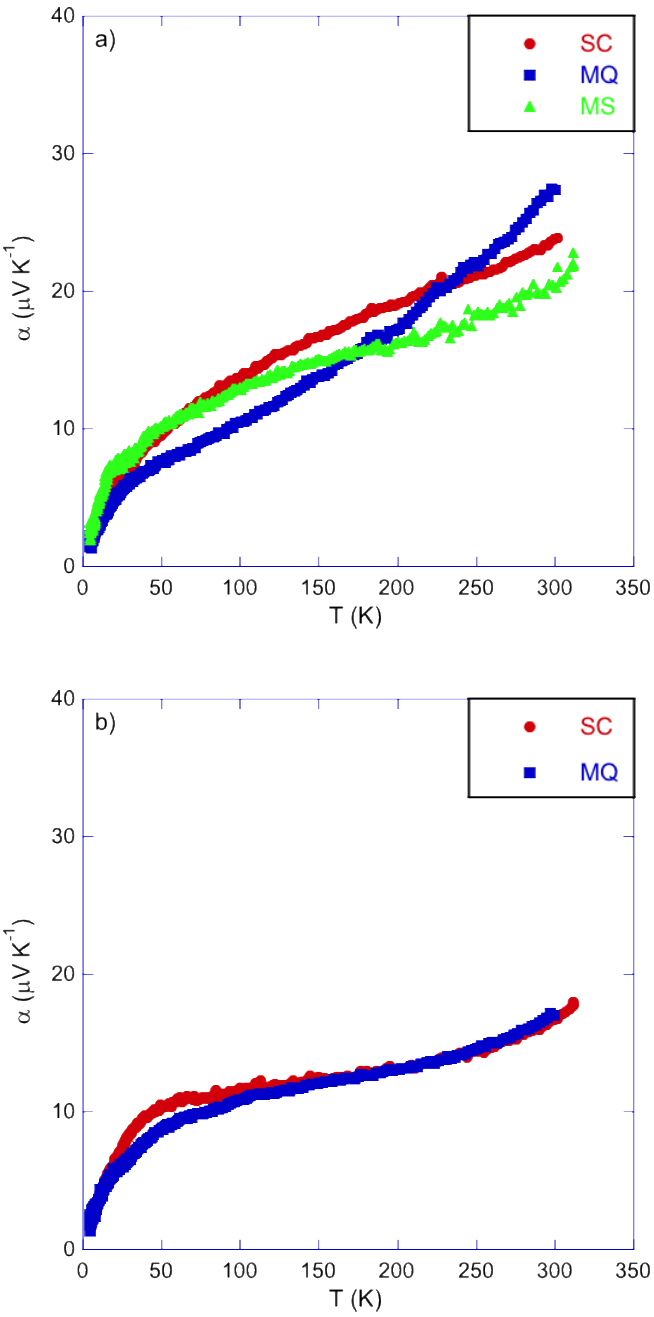
a)
SC
MQ
MS
α (μV K^{-1})
T (K)
0
10
20
30
40
0
50
100
150
200
250
300
350
b)
SC
MQ
α (μV K^{-1})
T (K)

Figure 4

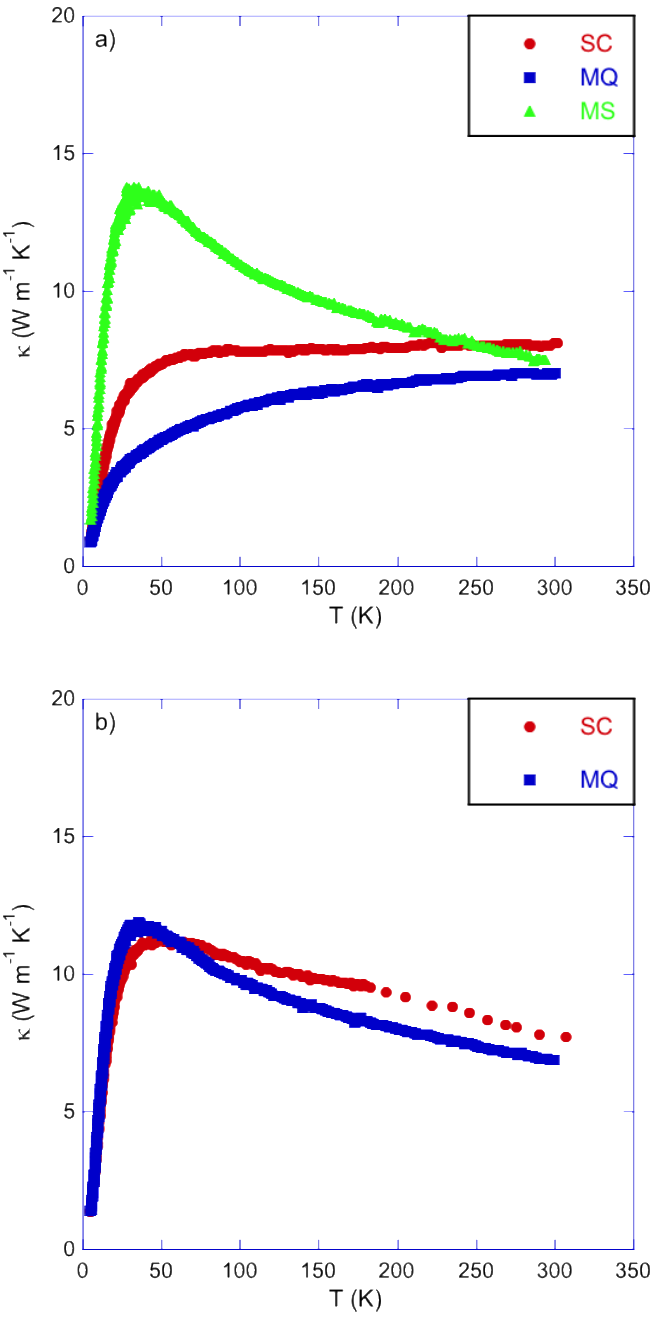

Figure 5

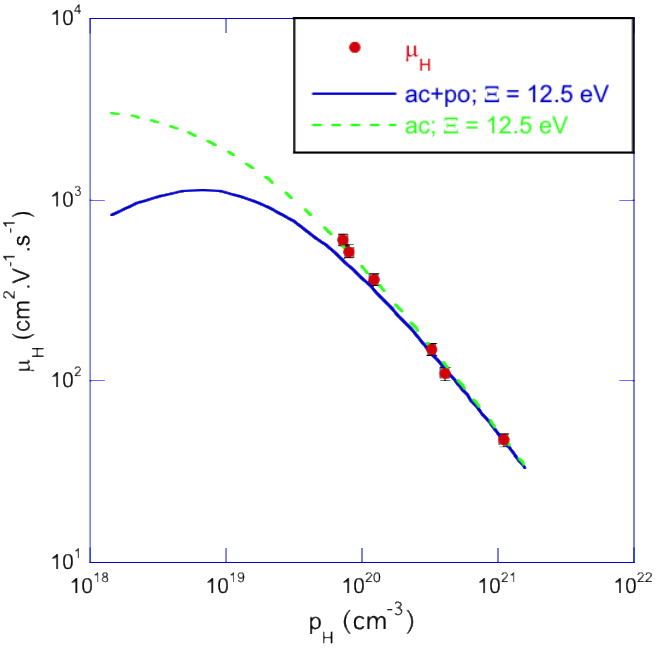
μH
ac+po; Ξ = 12.5 eV
ac; Ξ = 12.5 eV
μH (cm2.V-1.s-1)
pH (cm-3)
10^4
10^3
10^2
10^1
10^18
10^19
10^20
10^21
10^22

Figure 6

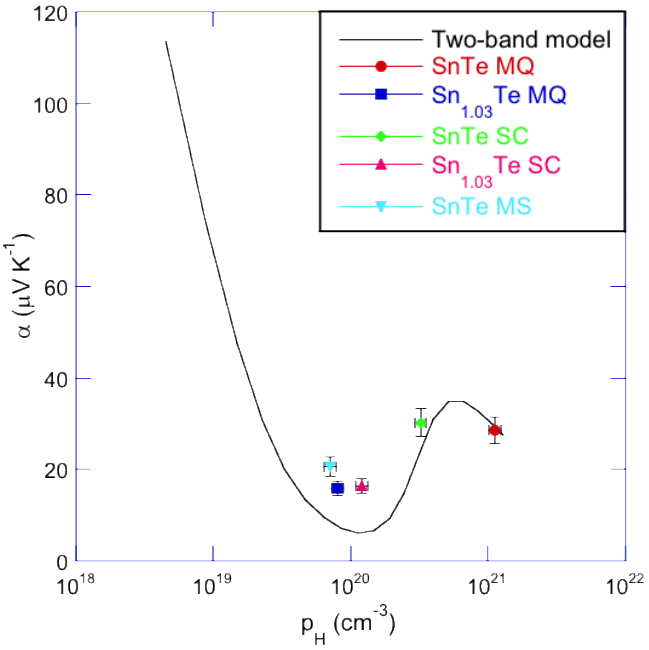
Two-band model
SnTe MQ
Sn1.03Te MQ
SnTe SC
Sn1.03Te SC
SnTe MS
α (μV K-1)
pH (cm-3)
120
100
80
60
40
20
0
10^18
10^19
10^20
10^21
10^22

Figure 7

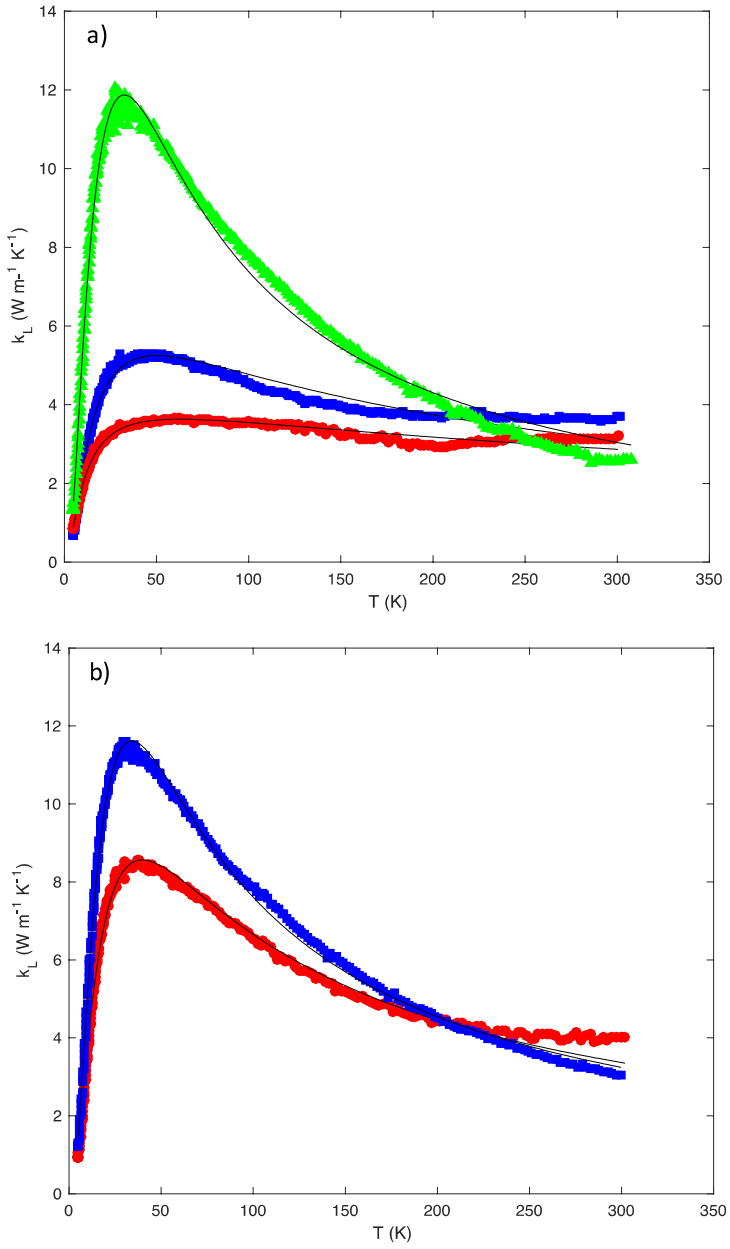

Figure 8

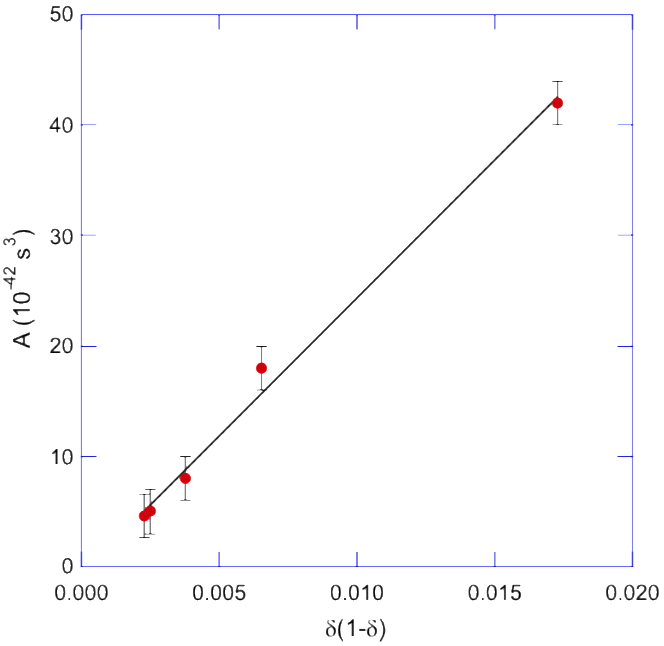

Figure 9